2005

Rheological and Structural Studies of Liquid Decane, Hexadecane, and Tetracosane under Planar Elongational Flow Using Nonequilibrium Molecular-dynamics Simulations

David J. Keffer
University of Tennessee - Knoxville

C. Baig
University of Tennessee - Knoxville

B. J. Edwards
University of Tennessee - Knoxville

H. D. Cochran
University of Tennessee - Knoxville

Recommended Citation
C. Baig, B. J. Edwards, D. J. Keffer, and H. D. Cochran, J. (2005). Rheological and structural studies of liquid decane, hexadecane, and tetracosane under planar elongational flow using nonequilibrium molecular-dynamics simulations. Chem. Phys. 122, DOI: 10.1063/1.1897373

Rheological and structural studies of liquid decane, hexadecane, and tetracosane under planar elongational flow using nonequilibrium molecular-dynamics simulations

C. Baig, B. J. Edwards,[a] D. J. Keffer, and H. D. Cochran
Department of Chemical Engineering, University of Tennessee, Knoxville, Tennessee 37996-2200

(Received 10 January 2005; accepted 2 March 2005; published online 11 May 2005)

We report for the first time rheological and structural properties of liquid decane, hexadecane, and tetracosane using nonequilibrium molecular-dynamics (NEMD) simulations under planar elongational flow (PEF). The underlying NEMD algorithm employed is the so-called *p*-SLLOD algorithm [C. Baig, B. J. Edwards, D. J. Keffer, and H. D. Cochran, J. Chem. Phys. **122**, 114103 (2005)]. Two elongational viscosities are measured, and they are shown not to be equal to each other, indicating two independent viscometric functions in PEF. With an appropriate definition, it is observed that the two elongational viscosities converge to each other at very low elongation rates, i.e., in the Newtonian regime. For all three alkanes, tension-thinning behavior is observed. At high elongation rates, chains appear to be fully stretched. This is supported by the result of the mean-square end-to-end distance of chains $\langle R^2_{\mathrm{ete}}\rangle$ and the mean-square radius of gyration of chains $\langle R^2_g\rangle$, and further supported by the result of the intramolecular Lennard-Jones (LJ) potential energy. It is also observed that $\langle R^2_{\mathrm{ete}}\rangle$ and $\langle R^2_g\rangle$ show a different trend as a function of strain rate from those in shear flow: after reaching a plateau value, $\langle R^2_{\mathrm{ete}}\rangle$ and $\langle R^2_g\rangle$ are found to increase further as elongation rate increases. A minimum in the hydrostatic pressure is observed for hexadecane and tetracosane at about $\dot{\varepsilon}(m\sigma^2/\varepsilon)^{1/2}=0.02$. This phenomenon is shown to be associated with the intermolecular LJ potential energy. The bond-bending and torsional energies display similar trends, but a different behavior is observed for the bond-stretching energy. An important observation common in these three bonded-intramolecular interactions is that all three modes are suppressed to a small value at high elongation rates. We conjecture that a liquid-crystal-like, nematic structure is present in these systems at high elongation rates, which is characterized by a strong chain alignment with a fully stretched conformation. © *2005 American Institute of Physics*.
[DOI: 10.1063/1.1897373]

I. INTRODUCTION

Understanding rheological and structural behaviors of polymeric materials in flowing systems is important not only in practical polymer processing but also in advancing our knowledge of the fundamental characteristics of chain molecules, i.e., viscoelasticity.[1,2] There exist two important standard flows in rheology:[2] shear flow (e.g., planar Couette flow and Hagen–Poiseuille flow) and elongational flow [e.g., uniaxial elongational flow (UEF), biaxial elongational flow (BEF), and planar elongational flow (PEF)].

Because of its amenability, numerous experimental data of shear flow have been published in the literature.[1,2] Furthermore, successful development of proper nonequilibrium molecular-dynamics (NEMD) simulation algorithms[3–6] for shear flow has made it possible not only to produce important rheological and structural properties for a system condition at which a real experiment is difficult to perform but also to understand the fundamental nature of chain molecules by observing their dynamics under flow at atomistic time and length scales.

The other important standard flow is elongational flow. In contrast with shear flow, it is extremely difficult to perform real experiments in elongational flow, and thus only a few experimental data are available for this flow field.[2] Research is still in progress toward developing improved experimental apparatus and methodologies for measuring elongational viscosities.[2] In this regard, without doubt, the computational feasibility of simulating elongational flows would be tremendously helpful. Unfortunately, NEMD simulations of elongational flow, in particular, for chain molecules with a long relaxation time, have been limited by the simulation time, since at least one dimension is contracting with time in this flow. This problem has been partially resolved by Kraynik and Reinelt's[7] ingenious discovery of the temporal and spatial periodicity of lattice vectors in PEF. (Unfortunately, these authors also proved that no such periodicity exists for UEF and BEF.) Using their idea, there have been a few partially successful NEMD simulations of PEF for simple fluids using the so-called SLLOD (Refs. 5,6) algorithm.[8,9] These simulation works demonstrated successful application of the Kraynik–Reinelt boundary conditions (KRBCs) in computer simulations of PEF.

Very recently, however, Todd and Daivis[10] have reported another serious problem in *NVT* NEMD simulations of PEF

[a]Author to whom correspondence should be addressed. Electronic mail: bjedwards@chem.engr.utk.edu

when using the SLLOD algorithm. Regardless of the thermostat (Nosé–Hoover or Gaussian), the size of the time step (small or large), the dimensionality of the fluids (two or three dimensional), or the integration scheme (Gear predictor-corrector or velocity Verlet), the total linear momentum in the contracting direction grows exponentially, which results in an aphysical phase transition after a certain time interval. This phenomenon starts from a nonzero initial total linear momentum of the system due to the limit of numerical precision (truncation error) in computer simulations. Accepting this source of error as numerically unavoidable, the underlying cause should be ascribed to the basic algorithm used in the simulations.

This problem has been completely resolved by the present authors[11] using the so-called proper-SLLOD (or *p*-SLLOD) algorithm. The *p*-SLLOD algorithm was originally proposed by Tuckerman *et al.*,[12] and later derived by Edwards and Dressler[13] through a fundamental investigation of the canonical structure of the evolution equations under a completely Hamiltonian perspective. In the authors' recent paper,[11] the fundamental correctness of the *p*-SLLOD algorithm was further demonstrated through a detailed analysis of all the existing NEMD algorithms (DOLLS, SLLOD, and *p*-SLLOD). Only the *p*-SLLOD algorithm, in general, i.e., for any type of flow, satisfies two fundamental criteria: Newtonian dynamics and thermodynamics. Based on the violation of Newtonian dynamics by a NEMD algorithm, it was also demonstrated why the DOLLS algorithm does not give correct results even for shear flow, but the SLLOD algorithm does so. (The SLLOD and *p*-SLLOD algorithms are identical for shear flow.) Furthermore, it was demonstrated that the SLLOD algorithm does not satisfy Newtonian dynamics in elongational flow, and thus should not be used in this flow. Finally, through NEMD simulations of PEF using the *p*-SLLOD algorithm, it was shown that one no longer encounters the aphysical phenomenon observed by Todd and Daivis with respect to the total momentum of the system. Interested readers should refer to the original paper.[11]

In the present work, we extend our simulation methodology for NEMD simulations of PEF from simple fluids to relatively short complex fluids. We explore three alkanes, $C_{10}H_{22}$ (decane), $C_{16}H_{34}$ (hexadecane), and $C_{24}H_{50}$ (tetracosane), which previously have been studied under shear flow.[14–16] Thus, an advantage of choosing the three alkanes is to compare NEMD simulation results of PEF and those of shear flow, i.e., compare zero-elongation-rate and zero-shear-rate viscosities. A NEMD simulation for these alkanes under shear flow was previously carried out by Cui *et al.*;[15] therefore, it appears to be most appropriate to choose the same state points (see Sec. II) as those used by these authors for comparison.

This paper is organized as follows. In Sec. II, we describe the simulation methodology employed in this work: the equations of motion of the *p*-SLLOD algorithm with a Nosé–Hoover thermostat, the potential model, and simulation conditions (state points, parameters of KRBCs, and so on). In Sec. III, we present our simulation results with a detailed microscopic interpretation. Finally, conclusions from this study are presented in Sec. IV.

II. SIMULATION METHODOLOGY

In this section, we present the details of simulation strategy. To avoid unnecessary repetition, however, we will not here present the theoretical and computational backgrounds of the *p*-SLLOD algorithm and the technical details associated with it; instead, we refer readers to our previous paper.[11]

The *p*-SLLOD equations of motion for *NVT* NEMD simulations of PEF using the Nosé–Hoover thermostat[17–19] are written as[11]

$$\begin{aligned}
\dot{\mathbf{q}}_{ia} &= \frac{\mathbf{p}_{ia}}{m_{ia}} + \mathbf{q}_{ia} \cdot \boldsymbol{\nabla}\mathbf{u}, \\
\dot{\mathbf{p}}_{ia} &= \mathbf{F}_{ia} - \mathbf{p}_{ia} \cdot \boldsymbol{\nabla}\mathbf{u} - m_{ia}\mathbf{q}_{ia} \cdot \boldsymbol{\nabla}\mathbf{u} \cdot \boldsymbol{\nabla}\mathbf{u} - \frac{p_\zeta}{Q}\mathbf{p}_{ia}, \\
\dot{s} &= \frac{p_\zeta}{Q}, \\
\dot{p}_\zeta &= \sum_i \sum_a \frac{\mathbf{p}_{ia}^2}{m_{ia}} - DNk_BT,
\end{aligned} \tag{1}$$

where $\mathbf{p}_{ia}$ and $\mathbf{q}_{ia}$ are the momentum and position vectors of atom a in molecule i, respectively, $\mathbf{F}_{ia}$ is the force on atom a in molecule i of mass m_{ia}, and V is the system volume. D denotes dimensionality, N, the total number of atoms, T, the absolute temperature, and k_B, the Boltzmann constant, ζ and p_ζ are coordinate- and momentum-like variables of the Nosé–Hoover thermostat, respectively, and $Q=DNk_BT\tau^2$ is the mass parameter of the thermostat.

The potential model employed for our systems is essentially the same as that used by Cui *et al.*[15] for shear flow. The model was proposed by Siepmann *et al.*,[20] and is known as the Siepmann-Karaboni-Smit (SKS) united-atom model, with the exception that the rigid bond is replaced by a flexible one with harmonic potential. In this model, nonbonded intermolecular and intramolecular atom-atom (or site-site) interactions are modeled by the well-known Lennard-Jones (LJ) potential,

$$V_{\mathrm{LJ}}(r) = 4\varepsilon_{ij}\left[\left(\frac{\sigma_{ij}}{r}\right)^{12} - \left(\frac{\sigma_{ij}}{r}\right)^{6}\right], \tag{2}$$

where $\varepsilon_{ij}=(\varepsilon_i\varepsilon_j)^{1/2}$ and $\sigma_{ij}=(\sigma_i+\sigma_j)/2$ are the energy and size parameters of the LJ potential between atoms i and j. The parameters ε and σ are chosen as 47 K and 3.93 Å for the CH_2 group, and 114 K and 3.93 Å for the CH_3 group. In this work, we employed $2.5\sigma_{CH_2}$ for the cut-off distance.

The intramolecular LJ interaction is only active between atoms separated by more than three bonds. The bond-stretching interaction is modeled by a harmonic potential,

$$V_{\mathrm{str}}(l) = \frac{1}{2}k_{\mathrm{str}}(l - l_{\mathrm{eq}})^2, \tag{3}$$

where the bond-stretching constant $k_{\mathrm{str}}/k_B=452\,900$ K/Å and the equilibrium length $l_{\mathrm{eq}}=1.54$ Å. The bond-bending interaction is also governed by a harmonic potential,

TABLE I. Elongational viscosities η_1 and η_2 as functions of elongation rate for decane, hexadecane, and tetracosane. Numbers in parentheses represent the statistical uncertainties in the least significant digits calculated using Eq. (28) in Ref. 23.

		$C_{10}H_{22}$		$C_{16}H_{34}$		$C_{24}H_{50}$	
$\dot{\varepsilon}(m\sigma^2/\varepsilon)^{1/2}$	Total run time (ns)	η_1 (cP)	η_2 (cP)	η_1 (cP)	η_2 (cP)	η_1 (cP)	η_2 (cP)
0.0005	37.6					2.43 (27)	2.75 (54)
0.001	28.2					2.17 (14)	2.34 (29)
0.002	21.2			1.18 (7)	1.05 (15)	2.38 (11)	1.99 (18)
0.004	14.1	0.638 (34)	0.638 (76)	1.22 (5)	1.06 (9)	2.24 (6)	1.84 (9)
0.01	9.4	0.647 (21)	0.664 (34)	1.14 (2)	0.989 (39)	1.96 (3)	1.30 (5)
0.02	9.4	0.614 (12)	0.601 (18)	1.07 (2)	0.901 (23)	1.56 (2)	1.03 (4)
0.04	6.0	0.586 (7)	0.569 (12)	0.898 (6)	0.717 (15)	1.17 (1)	0.771 (15)
0.05	6.0	0.569 (5)	0.532 (10)	0.832 (6)	0.663 (9)	1.07 (1)	0.701 (16)
0.08	6.0	0.519 (3)	0.481 (6)	0.707 (4)	0.558 (7)	0.872 (6)	0.582 (9)
0.1	6.0	0.494 (3)	0.459 (5)	0.651 (3)	0.521 (6)	0.794 (4)	0.542 (7)
0.2	3.5	0.413 (2)	0.383 (3)	0.504 (2)	0.410 (4)	0.592 (3)	0.423 (5)
0.5	3.5	0.311 (1)	0.302 (2)	0.357 (1)	0.318 (2)	0.406 (1)	0.321 (2)
0.8	3.5	0.266 (1)	0.274 (2)	0.299 (1)	0.282 (2)	0.336 (1)	0.274 (2)
1.0	3.5	0.248 (1)	0.264 (1)	0.279 (1)	0.267 (2)	0.313 (1)	0.250 (2)

$$V_{\text{ben}}(\theta) = \frac{1}{2}k_{\text{ben}}(\theta - \theta_{\text{eq}})^2, \tag{4}$$

where the bond-bending constant $k_{\text{ben}}/k_B = 62\,500$ K/rad^2 and $\theta_{\text{eq}} = 114°$. The torsional interaction is described by the model proposed by Jorgensen *et al.*,[21]

$$V_{\text{tor}}(\phi) = \sum_{m=0}^{3} a_m(\cos\phi)^m, \tag{5}$$

where $a_0/k_B = 1010$ K, $a_1/k_B = 2019$ K, $a_2/k_B = 136.4$ K, and $a_3/k_B = -3165$ K.

The state points for decane, hexadecane, and tetracosane in this study are exactly the same as those used by Cui *et al.*[15] for shear flow: the temperature, $T = 298$ K, and the density, $\rho = 0.7247$ g/cm^3, for decane, $T = 323$ K and $\rho = 0.7530$ g/cm^3 for hexadecane, and $T = 333$ K and $\rho = 0.7728$ g/cm^3 for tetracosane. Exploring these states by NEMD simulations, we employed 200 molecules for decane, 162 molecules for hexadecane, and 100 molecules for tetracosane.

The equations of motion were integrated using the reversible reference system propagator algorithm (*r*-RESPA) developed by Tuckerman *et al.*[22] We devised the *r*-RESPA for PEF following the procedure by Tuckerman *et al.*[22] and Cui *et al.*[14] Two time scales are used; the large time step of 2.26 fs is used for the intermolecular interaction, and the small time step of 0.226 fs for the intramolecular interaction. The relaxation time parameter, τ, of the Nosé–Hoover thermostat was set equal to 0.24 ps. As for the KRBCs, we chose the Hencky strain, $\varepsilon_p \approx 0.9624$, and the initial orientation angle of the simulation box, $\theta_0 \approx 31.718°$, which are obtained by setting $k = 3$, $N_{11} = 2$, and $N_{12} = -1$ in Ref. 7. The time period, t_p for the KRBCs is determined from $\varepsilon_p = \dot{\varepsilon} t_p$. For details, readers are referred to the original paper.[7] As noted at the beginning of this section, for details of the implementation of the *p*-SLLOD algorithm with KRBCs for PEF, we refer readers to our previous paper.[11]

In this study, we used elongation rates in the range of $0.0005 \leqslant \dot{\varepsilon}(m\sigma^2/\varepsilon)^{1/2} \leqslant 1.0$. Because of the strong thermal Brownian motion of molecules overshadowing the external field effect, the three lowest elongation rates are omitted for decane, and the two lowest elongation rates for hexadecane. We suppose that the same situation was encountered by Cui *et al.*[15] in their work on shear flow for these short alkanes. In order to get more accurate results, i.e., smaller statistical uncertainties, we performed a sufficiently long simulation for each elongation rate, using longer simulations for smaller elongation rates. The details are presented in Table I. The statistical uncertainty for all the physical properties reported here was calculated using Eq. (28) in Ref. 23. Note that we did not include the error bars in the figures presented in this paper if the error bars of all the data in the figure are smaller than the size of the symbol used.

III. RESULTS AND DISCUSSION

In planar elongational flow, there exist two independent viscosity functions,[2,24] the first elongational viscosity, η_1, and the second elongational viscosity, η_2, defined as

$$\eta_1 = \frac{\Pi_{yy} - \Pi_{xx}}{4\dot{\varepsilon}}, \tag{6}$$

$$\eta_2 = \frac{\Pi_{yy} - \Pi_{zz}}{2\dot{\varepsilon}}. \tag{7}$$

Here, x is the direction of flow (extension), y is the direction of compression, and z is the neutral direction. The pressure tensor, Π, is calculated according to

$$\Pi = \left\langle \frac{1}{V}\sum_i \sum_a \left(\frac{\mathbf{p}_{ia}\mathbf{p}_{ia}}{m_{ia}} + \mathbf{q}_{ia}\mathbf{F}_{ia} \right) \right\rangle. \tag{8}$$

The angular brackets denote the time average of the system trajectory. The above definitions make it possible to compare η_1 and η_2 at low elongation rates, i.e., in the Newtonian

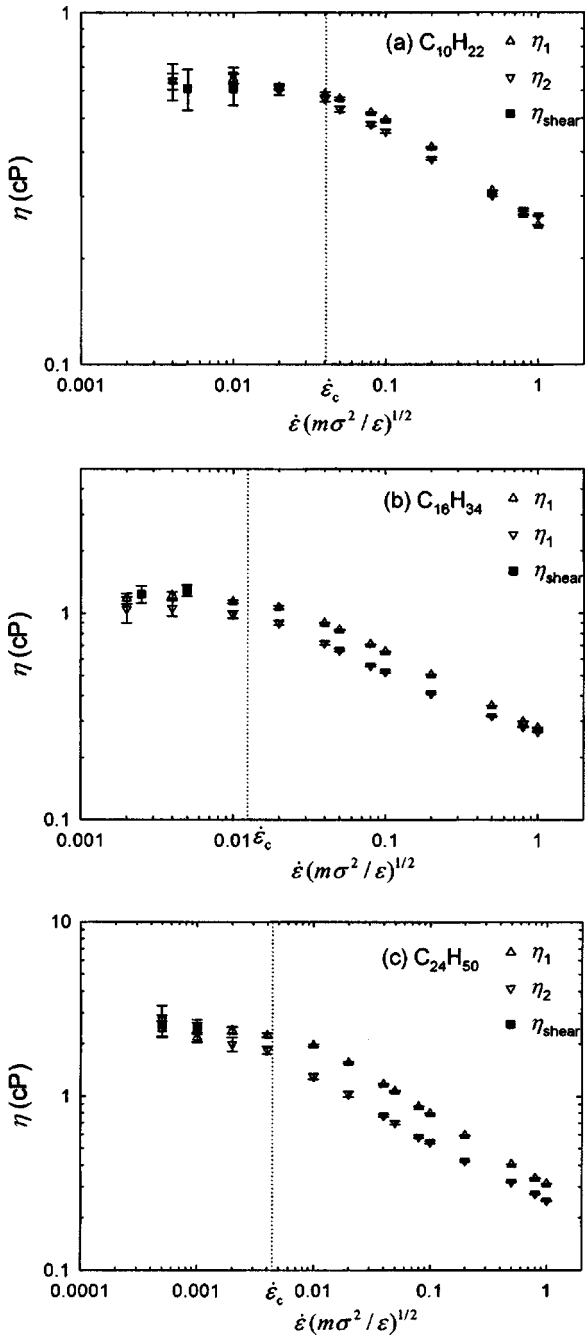

FIG. 1. Elongational viscosities η_1 and η_2 as functions of elongation rate for (a) decane, (b) hexadecane, and (c) tetracosane. Included are shear viscosities in the Newtonian regime at shear rates [as calculated by Cui *et al.* (Ref. 15)] corresponding to low elongation rates.

regime, and compare the elongational viscosities and shear viscosity at small strain rates.

In Table I, we present our NEMD simulation results of η_1 and η_2 as functions of elongation rate for the three alkanes. In Fig. 1, we plot η_1 and η_2 as functions of $\dot{\varepsilon}$. The vertical lines in the figure represent the "critical elongation rate," $\dot{\varepsilon}_c$, at which the product of a characteristic relaxation time λ and $\dot{\varepsilon}$ (note the Weissenberg number,[1] $\mathrm{We}=\lambda\dot{\varepsilon}$) is equal to unity, and which is often approximately considered as the boundary between the linear and the nonlinear regimes in flowing systems. We calculated the critical elongation rate based on the results of $\lambda=58$ ps for decane and $\lambda=531$ ps for tetracosane by Mondello and Grest,[25] and $\lambda=188$ ps for hexadecane by Cui *et al.*[15] Using those values, the reduced critical elongation rates are found to be $\dot{\varepsilon}_c(m\sigma^2/\varepsilon)^{1/2}=0.0406$, 0.0125, and 0.004 43 for decane, hexadecane, and tetracosane.

As shown in Fig. 1, for all three alkanes, both η_1 and η_2 decrease as elongation rate increases, i.e., tension-thinning behavior is observed. It is also observed that η_1 and η_2 are, in general, not equal to each other, indicating that there are two independent material functions. However, η_1 and η_2 at very low elongation rates, i.e., zero-elongation-rate viscosities for each system, appear to converge well to each other within the statistical uncertainties. As mentioned above, this behavior is evident because of the above rheological definition of η_1 and η_2. Furthermore, with this definition, the zero-elongation-rate viscosities, in principle, should be the same as the zero-shear-rate viscosity for shear flow. To show this, we included in the figure the shear viscosity at small strain rates reported by Cui *et al.*[15] It is seen in the figure that the two elongational viscosities at low elongational viscosities are approximately equal to the shear viscosities at low shear rates, within the statistical uncertainties. Based on our result at the lowest elongation rate for each alkane, we compare $\eta_1=0.64\pm0.03$ cP and $\eta_2=0.64\pm0.08$ cP with $\eta_{\mathrm{shear}}=0.61\pm0.08$ cP for decane, $\eta_1=1.18\pm0.07$ cP and $\eta_2=1.05\pm0.15$ cP with $\eta_{\mathrm{shear}}=1.24\pm0.12$ cP for hexadecane, and $\eta_1=2.43\pm0.27$ cP and $\eta_2=2.75\pm0.54$ cP with $\eta_{\mathrm{shear}}=2.56\pm0.35$ cP for tetracosane.

To compare the elongational viscosities of decane, hexadecane, and tetracosane with respect to elongation rate, we plot η_1 and η_2 separately in Fig. 2. Consistent with a well-known fact in polymer physics, both η_1 and η_2 are shown to become larger as the chain length increases. While there is clearly a significant difference between the elongational viscosities of the three alkanes at low elongational rates, the difference appears to decrease with elongation rate. This indicates that, even for these relatively short chain molecules, the tension-thinning behavior becomes more pronounced for the longer chain. Notice also that the difference in η_1 is reduced faster than that in η_2.

Figure 3 shows the effect of elongation on the hydrostatic pressure at constant density. For decane, the hydrostatic pressure increases monotonically with increasing elongation rate. For hexadecane, however, the opposite behavior is observed at low elongation rates with hydrostatic pressure eventually reaching a slight minimum value at $\dot{\varepsilon}(m\sigma^2/\varepsilon)^{1/2}=0.02$. At higher elongation rates, the pressure increases with elongation rate as in decane. This same phenomenon is more obvious in the case of tetracosane, where we clearly see a minimum of the pressure at $\dot{\varepsilon}(m\sigma^2/\varepsilon)^{1/2}=0.02$, below which it decreases with elongation rate, and above which it increases. This minimum behavior in the hydrostatic pressure has also been observed in NEMD simulations of shear flow for linear alkanes $C_{16}H_{34}$ and $C_{28}H_{58}$ by Khare *et al.*,[16] and $C_{100}H_{202}$ by Moore *et al.*[26] Another interesting observation for tetracosane is that the pressure appears to reach a plateau value at very high elongation rates.

To understand all of these observations, it is useful to consider them from a microscopic viewpoint. The contribu-

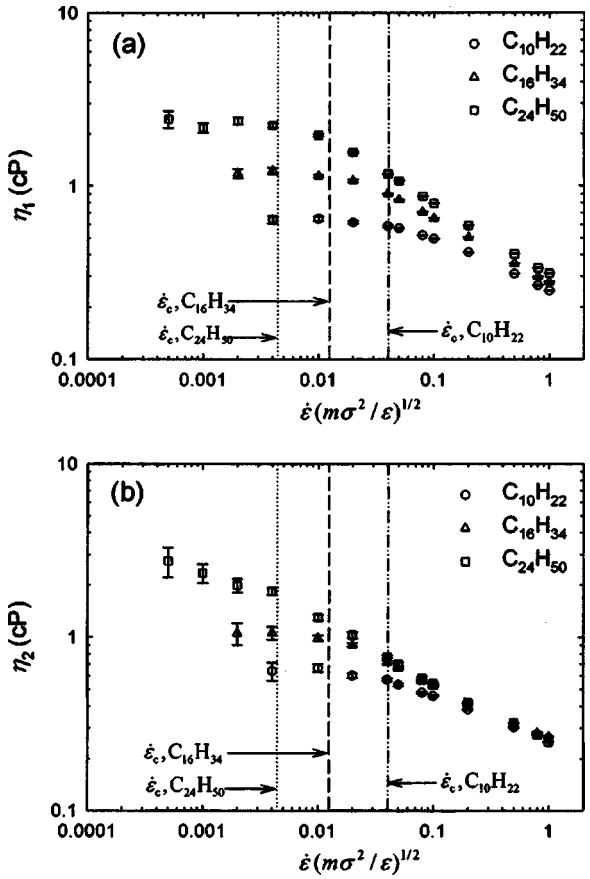

FIG. 2. Comparison of (a) η_1 and (b) η_2 vs elongation rate among decane, hexadecane, and tetracosane.

tion of the external flow field to the hydrostatic pressure appears in the potential part of the pressure tensor since the kinetic part is already determined by the imposed temperature. The change of the potential part of the pressure is supposed to result mostly from the change of the intermolecular interaction accompanying the change in the individual chain conformations and their arrangement in the system. Therefore, it seems to be appropriate to investigate the change of the intermolecular potential energy due to elongation.

In Fig. 4, we plot the intermolecular LJ potential energy

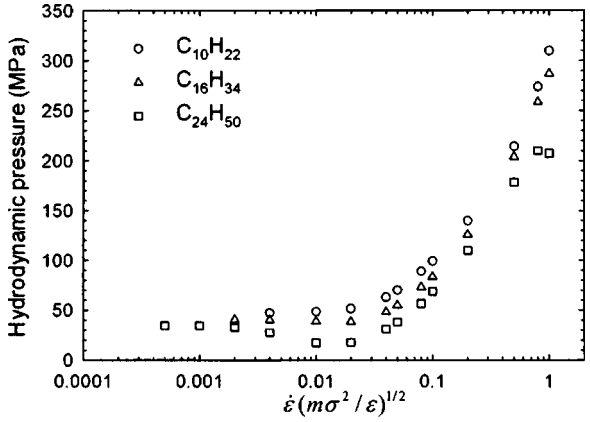

FIG. 3. Hydrostatic pressure vs elongation rate for decane, hexadecane, and tetracosane. The error bars of all data are smaller than the size of the symbols.

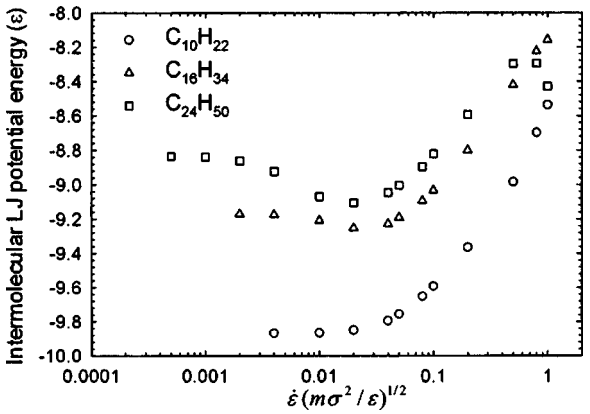

FIG. 4. Intermolecular LJ potential energy per united atom vs elongation rate for decane, hexadecane, and tetracosane. The error bars of all data are smaller than the size of the symbols.

per particle as a function of elongation rate. As shown in the figure, the overall shape of the intermolecular potential energy as a function of elongation rate for each alkane appears to be very similar to that of the pressure shown in Fig. 3. While there is shown to be no minimum of the intermolecular energy for decane, minima do exist at $\dot{\varepsilon}(m\sigma^2/\varepsilon)^{1/2} = 0.02$ for hexadecane and tetracosane. More interestingly, similar to the pressure of tetracosane displayed in Fig. 3, a plateau value of the intermolecular energy is observed at very high elongation rates.

Now let us consider the molecular origin of this behavior in Fig. 4 more carefully. In the presence of an elongational flow field, chains will tend to align themselves along the direction of flow. This has been directly verified by our simulation results. The shape of individual chains will also be distorted, i.e., elongated in the direction of flow. This alignment of chains with elongated conformations would increase the interaction area between molecules, and so strengthen the degree of intermolecular interaction. Therefore, this would result in a decrease of the intermolecular LJ potential energy of system, i.e., make the intermolecular potential energy more negative. Note again that the alignment angle is along the direction of flow in PEF, as has been directly verified via simulation.

With respect to the chain conformations, it is expected that as the elongation rate increases, the intramolecular structure of alkanes will be elongated more and more, and eventually become a fully stretched zigzag shape almost entirely in the *trans*-conformation at very high elongation rates. The fully stretched chains aligned with each other would give the most favorable intermolecular interaction in a static sense.

In a dynamic sense, we need also to consider the intermolecular collisions between molecules. Physically, it is likely that the elongational field in PEF induces intermolecular collisions. In contrast with the above alignment effect with elongated shape, these molecular collisions will increase the energy. In short, there are expected to be two competing factors involved with the intermolecular interaction. We note that the effect of collision has also been suggested by Moore *et al.*[26]

With the understanding that chain alignment lowers the intermolecular interaction energy while collisions raise it, let

us return to the intermolecular LJ potential energy in Fig. 4. At low elongation rates, the energy decreases with elongation rate because of the alignment of molecules along the direction of flow with elongated shape and the weak intermolecular collision compared with the effect of alignment. However, as elongation rate increases, the intermolecular collisions become stronger and become comparable to the effect of alignment, leading to an energy minimum at elongation rate $\dot{\varepsilon}(m\sigma^2/\varepsilon)^{1/2}=0.02$ for the present systems, as shown in Fig. 4. With a further increase of elongation rate, the collision effect is increased further and dominates the alignment effect. In this intermediate range of elongational rates, the alignment interaction would continue to increase due to the larger degree of alignment with more elongated shape; however, the alignment effect would not change enough to compensate for the collision effect. As mentioned above, however, a further increase of elongation rate will eventually lead to fully stretched, fully aligned chains. It is seen in Fig. 4 that this change of molecular structure indeed appears to occur at high elongation rates, such as $\dot{\varepsilon}(m\sigma^2/\varepsilon)^{1/2}=0.5$. This effect of the structural change will become more pronounced as the chain length increases because longer molecules can elongate to a greater extent.

A particularly strong effect due to the structural change occurs in tetracosane at high elongation rate so as to compete with the strong intermolecular collision, which thus explains the observation of a plateau for tetracosane on the hydrostatic pressure and intermolecular LJ potential-energy profiles, shown in Figs. 3 and 4, respectively. Although such a plateau does not appear explicitly in decane and hexadecane because even such a significant structural change is not yet strong enough to compete with the collision effect, the structural effect is still seen in the figures by estimating changes in magnitude at high elongation rates.

Also notice in Fig. 4 that the intermolecular LJ potential energy seems to decrease at the highest elongation rate employed in this work after reaching the plateau. At this point, although it is difficult to give a definite answer without a further investigation on higher elongation rates (without a possible thermostat artifact[6]), we conjecture that the structural effect will reach its maximum value at a certain high elongation rate with a maximum alignment with the fully stretched conformation, and after the maximum stage, it would not change anymore, but be constant with a further increase of elongation rate. In contrast, the intermolecular collision is expected to still increase with increasing elongation rate after the maximum stage. Therefore, we conjecture with caution that the hydrostatic pressure and the intermolecular LJ energy of tetracosane, shown in Figs. 3 and 4, respectively, would eventually increase further at the higher elongation rates.

Now let us examine two important structural quantities, the mean-square end-to-end distance of chains, $\langle R_{\mathrm{ete}}^2\rangle$, and the mean-square radius of gyration of chains, $\langle R_g^2\rangle$. Since both $\langle R_{\mathrm{ete}}^2\rangle$ and $\langle R_g^2\rangle$ are directly related to the molecular conformations, they are expected to show a similar behavior with varying strength of field. This expectation is indeed observed in Fig. 5. $\langle R_{\mathrm{ete}}^2\rangle$ and $\langle R_g^2\rangle$ show almost the same behavior qualitatively as functions of elongation rate. A

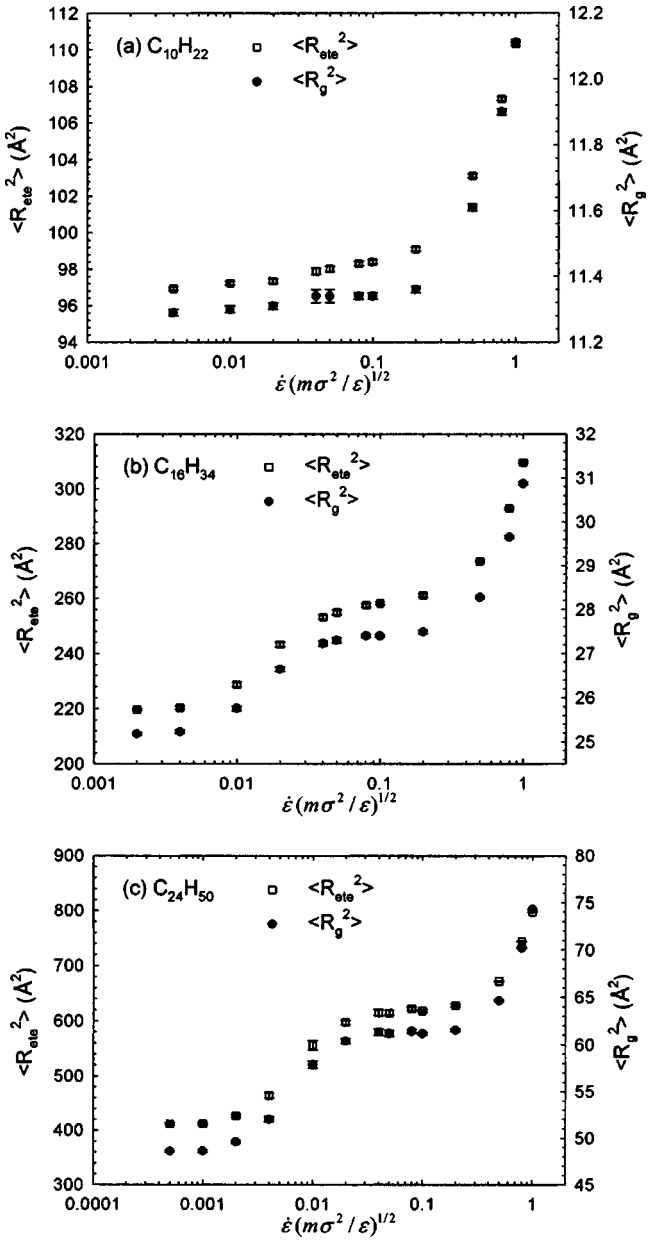

FIG. 5. The mean-square chain end-to-end distance, $\langle R_{\mathrm{ete}}^2\rangle$, and the mean-square chain radius of gyration, $\langle R_g^2\rangle$, vs elongation rate for (a) decane, (b) hexadecane, and (c) tetracosane.

quantitative comparison needs a more detailed theoretical analysis. (Quantitative results for these entities are presented in Table II.) While the overall shapes of $\langle R_{\mathrm{ete}}^2\rangle$ and $\langle R_g^2\rangle$ as functions of elongation rate look different from that of the hydrostatic pressure shown in Fig. 3, we may attribute the behavior of $\langle R_{\mathrm{ete}}^2\rangle$ and $\langle R_g^2\rangle$ to the same molecular origin as that of the pressure. At low elongation rates, both $\langle R_{\mathrm{ete}}^2\rangle$ and $\langle R_g^2\rangle$ increase with increasing elongation rate because the molecules are elongated due to the field. In the intermediate range of elongation rate, the intermolecular collisions become stronger. The strong collision between molecules is likely to disrupt their full elongation.

This phenomenon can be more easily understood based on the mean-field concept. Let us consider a single chain under a hypothetical field action, which exerts random impulses on the particles of the chain. In this environment, the

TABLE II. The mean-square end-to-end distance of chains, $\langle R_{ete}^2 \rangle$, and the mean-square radius of gyration of chains, $\langle R_g^2 \rangle$, as functions of elongation rate for decane, hexadecane, and tetracosane. Numbers in parentheses represent the statistical uncertainties in the least significant digits calculated using Eq. (28) in Ref. 23.

		$C_{10}H_{22}$		$C_{16}H_{34}$		$C_{24}H_{50}$	
$\dot{\varepsilon}(m\sigma^2/\varepsilon)^{1/2}$	Total run time (ns)	$\langle R_g^2 \rangle$ (Å^2)	$\langle R_{ete}^2 \rangle$ (Å^2)	$\langle R_g^2 \rangle$ (Å^2)	$\langle R_{ete}^2 \rangle$ (Å^2)	$\langle R_g^2 \rangle$ (Å^2)	$\langle R_{ete}^2 \rangle$ (Å^2)
0	6.4	11.30 (2)	97.06 (14)	25.18 (4)	219.5 (6)	48.36 (32)	408.2 (50)
0.0005	37.6					48.57 (12)	411.3 (17)
0.001	28.2					48.60 (12)	411.8 (19)
0.002	21.2			25.18 (3)	219.7 (4)	49.59 (18)	426.6 (27)
0.004	14.1	11.29 (1)	96.93 (9)	25.23 (4)	220.4 (6)	52.02 (30)	464.4 (47)
0.01	9.4	11.30 (1)	97.23 (11)	25.76 (5)	228.7 (8)	57.90 (38)	556.0 (86)
0.02	9.4	11.31 (1)	97.34 (12)	26.65 (5)	243.3 (8)	60.38 (26)	597.3 (39)
0.04	6.0	11.34 (2)	97.88 (17)	27.23 (6)	253.2 (8)	61.34 (33)	615.1 (55)
0.05	6.0	11.34 (2)	98.01 (15)	27.30 (6)	254.9 (8)	61.19 (32)	614.5 (44)
0.08	6.0	11.34 (1)	98.31 (12)	27.40 (4)	257.5 (6)	61.42 (19)	621.7 (29)
0.1	6.0	11.34 (1)	98.40 (11)	27.40 (3)	258.2 (5)	61.16 (13)	618.4 (20)
0.2	3.5	11.36 (1)	99.09 (11)	27.49 (4)	261.1 (6)	61.54 (15)	628.0 (23)
0.5	3.5	11.61 (1)	103.1 (1)	28.27 (3)	273.5 (4)	64.62 (8)	671.8 (11)
0.8	3.5	11.90 (1)	107.3 (1)	29.65 (3)	292.9 (4)	70.20 (5)	744.2 (7)
1.0	3.5	12.11 (1)	110.3 (1)	30.87 (3)	309.6 (4)	74.31 (4)	797.1 (5)

chain would have a smaller extension rather than its full extension without the hypothetical field. In short, the intermolecular collisions inhibit the full elongation of the chain structure. These two competing factors of collision and elongation result in a plateau value in $\langle R_{ete}^2 \rangle$ and $\langle R_g^2 \rangle$, as shown in Fig. 5. It is also seen that the plateaus are reached at about $\dot{\varepsilon}(m\sigma^2/\varepsilon)^{1/2}=0.02$, at which point the hydrostatic pressure and intermolecular potential energy reach their minima, as shown in Figs. 3 and 4, respectively. Above this intermediate range, a further increase of elongation rate will lead eventually to fully stretched chains.

Up to now, our microscopic interpretation seems to be physically reasonable and consistent. This physical picture can be further supported by the plot of the intramolecular LJ potential energy, which is shown in Fig. 6. As expected, comparing Figs. 5 and 6, it is seen that there is a close relationship among $\langle R_{ete}^2 \rangle$, $\langle R_g^2 \rangle$, and the intramolecular LJ energy.

We may further understand the effect of elongation on the intramolecular LJ energy through the consideration of the chain flexibility. The overall chain flexibility is governed by the torsional interaction. The fully stretched chain conformation may be considered as a very stiff chain with a zigzag shape, i.e., with the energetically favorable *trans*-conformation along the chain, and, therefore, the torsional energy is expected to be very low. On the other hand, this stretched conformation will increase the intramolecular LJ potential energy (or make it less negative) because the atoms in the same chain are separated from each other by greater distances. This physical picture is indeed confirmed by comparing Figs. 6 and 7 at high elongation rates. Above $\dot{\varepsilon}(m\sigma^2/\varepsilon)^{1/2}=0.2$, the torsional energy is seen to decrease very steeply with increasing elongation rate, indicating that the chains become very stiff.

Another aspect worthy of consideration is that, at the fully stretched state, $\langle R_{ete}^2 \rangle$ would not even approximately

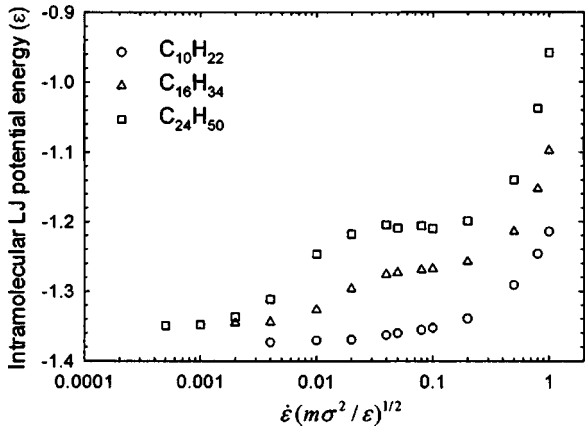

FIG. 6. Intramolecular LJ potential energy per united atom vs elongation rate for decane, hexadecane, and tetracosane. The error bars of all data are smaller than the size of the symbols. The number of united atoms in a chain is n for C_nH_{2n+2}.

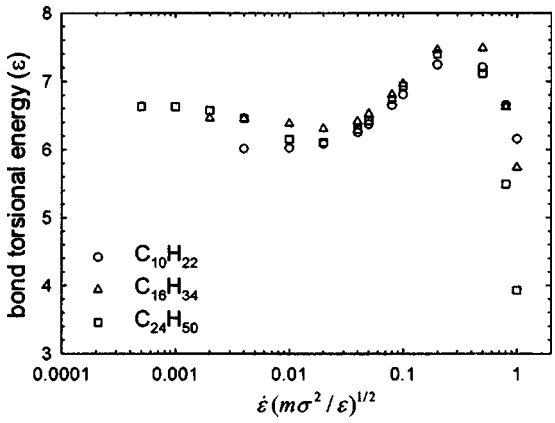

FIG. 7. Bond-torsional energy per mode vs elongation rate for decane, hexadecane, and tetracosane. The error bars of all data are smaller than the size of the symbols. The number of torsional modes in a chain is n-3 for C_nH_{2n+2}.

scale linearly with the chain length, but rather would scale quadratically with the chain length. The fully stretched state of chains at high elongation rates can be roughly confirmed by comparing the quantitative results of $\langle R_{ete}^2 \rangle$ at high elongation rates between alkanes in Table II. Of course, for a more exact quantitative comparison, one would need to include other contributions such as the bond-stretching and bond-bending modes.

It is also seen from Fig. 7 that the torsional energy decreases with elongation rate at low rates, then reaches a minimum value and increases at intermediate rates. All of these observations can be understood in the same way as above by considering the competing effects of intermolecular collision and elongated chain alignment.

For additional understanding of the variation of torsional energy with elongation rate, we investigated the distribution function of the torsional mode as a function of torsional angle for different elongation rates—see Fig. 8. It is quite instructive to compare Figs. 7 and 8 in detail. For example, for tetracosane shown in Fig. 8(c), the distribution function at the *trans*-state (or zero torsional angle) is increasing with increasing elongation rate at low rates up to $\dot{\varepsilon}(m\sigma^2/\varepsilon)^{1/2} = 0.02$. After that, at intermediate rates, it decreases with increasing elongation rate and reaches a minimum value, which corresponds to the maximum torsional energy in Fig. 7. Further increase of elongation rate brings about a higher value of the distribution function of the *trans*-state. Notice in Fig. 8 that the increase of the distribution function of the *trans*-state is accompanied by a decrease of the distribution function of the *gauche*-state and other states, which indicates that the chains get stiffer.

Based upon the structural information contained in Figs. 7 and 8, we conjecture that the fluid of flexible chains adopts a liquid-crystal-like, nematic structure, characterized by a strong chain alignment with a fully stretched conformation, at high elongation rates. This conjecture is supported by the results of other intramolecular interactions, i.e., bond bending and bond stretching.

To further understand the effect of elongation field on the chain structure, we also examined the bond-bending and bond-stretching modes. While the global chain flexibility is controlled mainly by the torsional interaction, the relatively short-range local chain flexibility would be determined by the bond-bending and even possibly the bond-stretching interactions. Figure 9 shows the variation of the bond-bending energy as a function of elongation rate. The plot of the bond-bending energy qualitatively resembles that of the torsional energy shown in Fig. 7. Thus, for this phenomenon, we may give the same physical interpretation as for the torsional energy.

Figure 10 shows the distribution function of the bond-bending mode with respect to the bending angle for different elongation rates. Initially at low elongational rates, the distribution appears to be broader and to reach a minimum at $\dot{\varepsilon}(m\sigma^2/\varepsilon)^{1/2} = 0.02$. After that, as the elongation rate increases, the distribution becomes narrower with a higher value of the peak. Physically, this means that the bond-bending motion becomes more and more restricted around the equilibrium angle; that is, chains get stiffer locally.

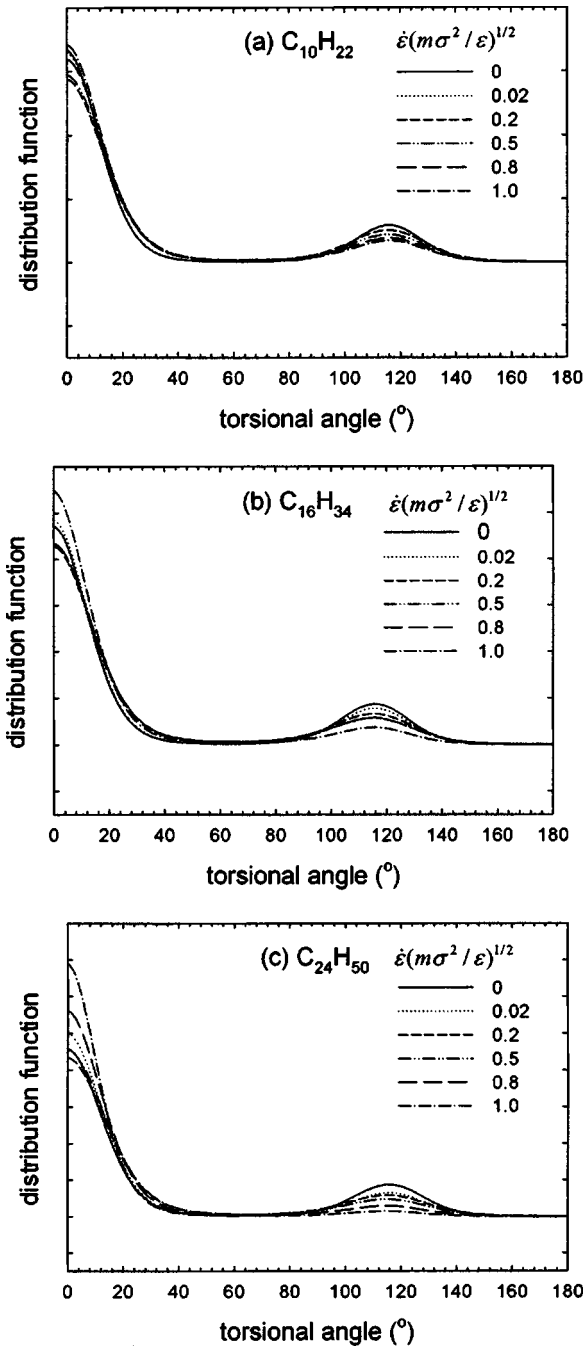

FIG. 8. The bond-torsional distribution function vs elongation rate for (a) decane, (b) hexadecane, and (c) tetracosane.

Therefore, at high elongation field, the chains become stiffer both globally and locally as the elongation rate increases.

Finally, the bond-stretching mode is shown in Fig. 11. The overall shape of the plot of the bond-stretching mode appears to be rather different from those of the torsional and the bond-bending modes. Neither a minimum nor a maximum is observed in the bond-stretching energy over the whole range of elongation rates. This seems to reflect the very strong force constant describing the bond-stretching mode compared with the relatively weak force constants describing the bond-bending and torsional modes. For the present systems of alkanes, a much greater energy is required to change the bond length than to alter bond or dihedral angles.

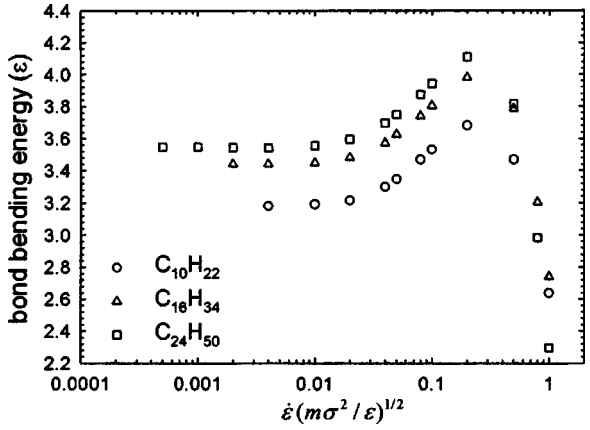

FIG. 9. Bond-bending energy per mode vs elongation rate for decane, hexadecane, and tetracosane. The error bars of all data are smaller than the size of the symbols. The number of bond-bending modes in a chain is n-2 for C_nH_{2n+2}.

We also conjecture that the change in $\langle R_{\mathrm{ete}}^2 \rangle$ and $\langle R_g^2 \rangle$ due to elongation, in general, does not result from the change of the bond length (at least in the range of elongation used in this study), but mainly from the decrease of the global flexibility determined by the torsional mode and possibly from the decrease of the local flexibility determined by the bond-bending mode. The latter effect is, however, expected to be much smaller than that of the torsional mode. Figure 11 shows that the bond-stretching energy decreases monotonically with increasing elongation rate over the whole range of $\dot{\varepsilon}$, and eventually reaches a very small value. The steep decrease of the bond-stretching energy at high elongation rates is also observed, as shown in the bond-bending and torsional energies. Physically, this means that at high elongation rates, the fluctuation of bond length about its equilibrium value becomes very small. This phenomenon is indeed confirmed by the result of the bond-stretching distribution function as a function of elongation rate. As shown in Fig. 12, the overall shape of the distribution function becomes steeper around the equilibrium bond length with increasing elongation rate. This result is exactly consistent with the observation of Fig. 11 and the above physical interpretation of smaller fluctuations of bond length with higher elongation rate.

In summary, all of the torsional, bond-bending, and bond-stretching motions are observed to be very much suppressed at high elongation rates. As mentioned before, it seems that at high elongation rates, the chains are highly aligned in a fully stretched conformation, and thus eventually form a liquid-crystal-like, nematic structure. We also note that in a strong elongational flow field, chains are very stiff and aligned with the direction of the field, and thus the motion of chains would not be isotropic as in the equilibrium state. Both the translational and orientational movements of chains in the direction perpendicular to the alignment direction are expected to be very restricted because of the geometrical constraint.[27] It would be rather easier to move in the direction parallel to the alignment direction. Here it is noted that even if chains are very stiff at this strong elongation field, the individual atoms along the chain still perform their thermal Brownian movements. Therefore, the overall chain

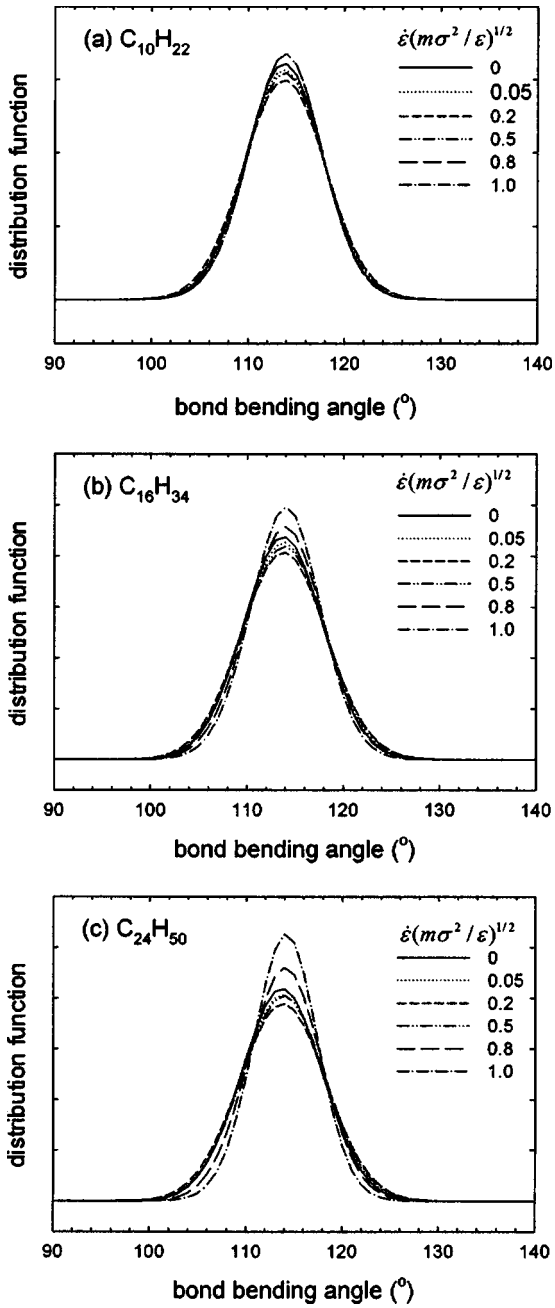

FIG. 10. The bond-bending distribution function vs elongation rate for (a) decane, (b) hexadecane, and (c) tetracosane.

movement is not the same as that of a rigid rod. In this situation, chains may take some sort of "reptating" movement[27,28] to a certain degree. Moore *et al.*[26] reported that their simulation results of $C_{100}H_{202}$ under shear were consistent with the reptation model[28] rather than the Rouse model.[29] This might be worthy of consideration when developing theories of chain dynamics under an elongational flow field.

IV. CONCLUSIONS

In this study, we have reported the rheological and structural properties of decane, hexadecane, and tetracosane under planar elongational flow for the first time. We investigated these properties in a systematic way using NEMD simula-

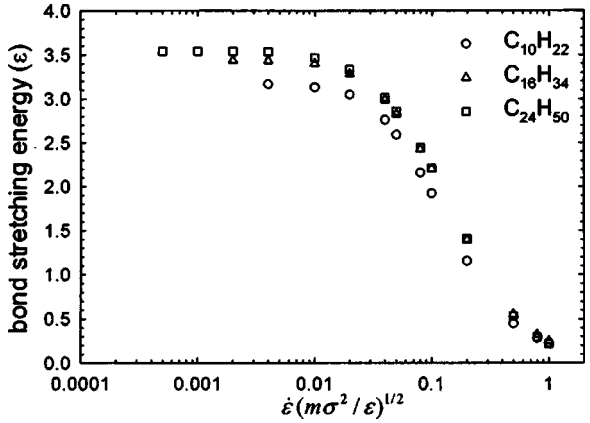

FIG. 11. Bond-stretching energy per mode vs elongation rate for decane, hexadecane, and tetracosane. The error bars of all data are smaller than the size of the symbols. The number of bond-stretching modes in a chain is n-1 for C_nH_{2n+2}.

tions implemented using the p-SLLOD algorithm. For each rheological and structural phenomena observed in this study under PEF, we provided a fairly detailed interpretation from the microscopic viewpoint. All of our explanations seem to be physically plausible and consistent. Some physical properties, such as the hydrostatic pressure, appeared to be qualitatively similar to those observed under shear,[15,16] but not so for all the properties.

Two elongational viscosities, η_1 and η_2, were separately calculated with appropriate rheological definitions. For all three alkanes, η_1 and η_2 showed a tension-thinning behavior as elongation rate increased. It was observed that η_1 and η_2 are, in general, not identical to each other, indicating that two independent viscometric functions actually exist. Consistent with the theoretical prediction, η_1 and η_2 appeared to converge to each other at low elongation rates, i.e., in the Newtonian regime. For the three alkanes, the zero-elongation-rate viscosities calculated in this work agreed well with the zero-shear-rate viscosities reported by Cui *et al.*[15] Another interesting similarity between shear[15,16] and planar elongational flows was found in that for both flows there exists a minimum in the hydrostatic pressure at constant density versus strain rate for these alkanes.

The mean-square end-to-end distance of chains $\langle R_{\mathrm{ete}}^2 \rangle$ and the mean-square radius of gyration of chains $\langle R_g^2 \rangle$ showed different trends from those in shear flow. After reaching a plateau value, $\langle R_{\mathrm{ete}}^2 \rangle$ and $\langle R_g^2 \rangle$ were shown to increase further as elongation rate increases. This phenomenon has been interpreted by conjecturing that chains are fully stretched at high elongational rates. This conjecture was well supported by the examination of the intramolecular LJ energy.

The effect of elongational flow on three bonded-intramolecular interactions (i.e., bond-stretching, bond-bending, and torsion) was investigated in detail with further help of the distribution functions. The bond-bending and torsional energies showed a similar trend to each other, but a different behavior was observed in the bond-stretching energy. An important observation common in these three interactions was that all three modes were suppressed to small

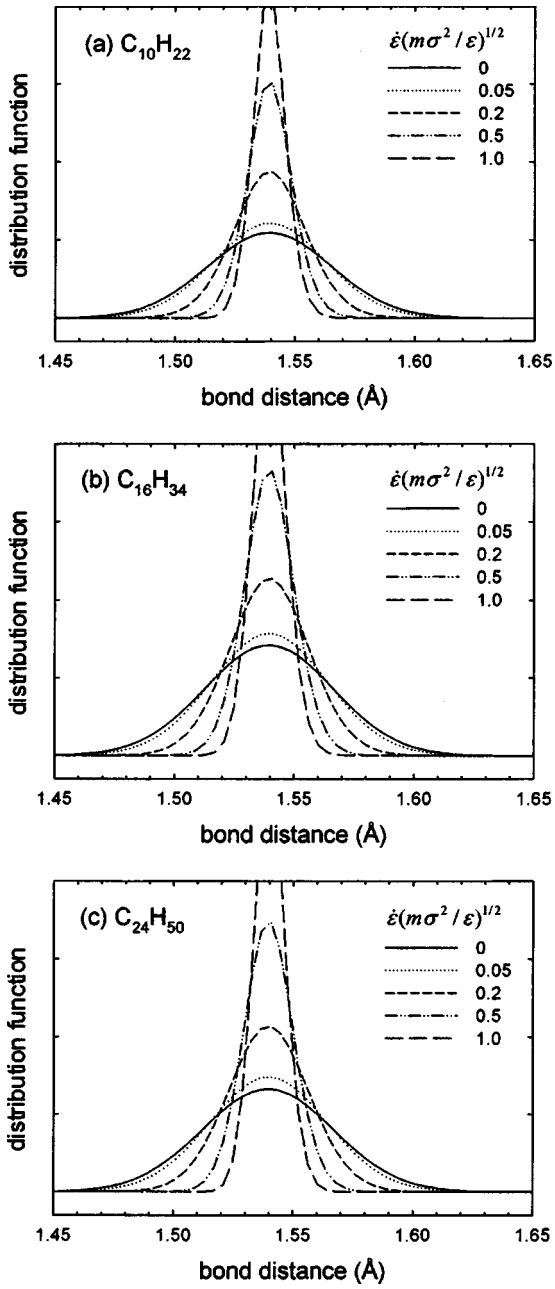

FIG. 12. The bond-stretching distribution function vs elongation rate for (a) decane, (b) hexadecane, and (c) tetracosane.

values at high elongation rates. We conjectured that a liquid-crystal-like, nematic structure, characterized by a strong chain alignment with a fully stretched conformation, exists in systems at high elongation rates.

ACKNOWLEDGMENTS

We would like to acknowledge helpful discussions with Dr. V. G. Mavrantzas and Dr. V. A. Harmandaris in the preparation of this work. This research was supported by the Division of Materials Sciences and Engineering of the U.S. Department of Energy (DOE) at Oak Ridge National Laboratory (ORNL) and through a subcontract at the University of Tennessee. This research used resources of the Center for Computational Sciences at Oak Ridge National Laboratory,

which is supported by the Office of Science of the DOE also under Contract No. DE-AC05-00OR22725.

[1]R. B. Bird, R. C. Armstrong, and O. Hassager, *Dynamics of Polymeric Liquids*, Fluid Mechanics, Vol. 1, 2nd ed. (Wiley-Interscience, New York, 1987).
[2]F. A. Morrison, *Understanding Rheology* (Oxford University Press, New York, 2001).
[3]A. W. Lees and S. F. Edwards, J. Phys. C **5**, 1921 (1972).
[4]W. G. Hoover, D. J. Evans, R. B. Hickman, A. J. C. Ladd, W. T. Ashurst, and B. Moran, Phys. Rev. A **22**, 1690 (1980).
[5]D. J. Evans and G. P. Morriss, Phys. Rev. A **30**, 1528 (1984).
[6]D. J. Evans and G. P. Morriss, *Statistical Mechanics of Nonequilibrium Liquids* (Academic, New York, 1990).
[7]A. M. Kraynik and D. A. Reinelt, Int. J. Multiphase Flow **18**, 1045 (1992).
[8]B. D. Todd and P. J. Daivis, Phys. Rev. Lett. **81**, 1118 (1998); Comput. Phys. Commun. **117**, 191 (1999).
[9]A. Baranyai and P. T. Cummings, J. Chem. Phys. **110**, 42 (1999).
[10]B. D. Todd and P. J. Daivis, J. Chem. Phys. **112**, 40 (2000).
[11]C. Baig, B. J. Edwards, D. J. Keffer, and H. D. Cochran, J. Chem. Phys. **122**, 114103 (2005).
[12]M. E. Tuckerman, C. J. Mundy, S. Balasubramanian, and M. L. Klein, J. Chem. Phys. **106**, 5615 (1997).
[13]B. J. Edwards and M. Dressler, J. Non-Newtonian Fluid Mech. **96**, 163 (2001).
[14]S. T. Cui, P. T. Cummings, and H. D. Cochran, J. Chem. Phys. **104**, 255 (1996).
[15]S. T. Cui, S. A. Gupta, P. T. Cummings, and H. D. Cochran, J. Chem. Phys. **105**, 1214 (1996).
[16]R. Khare, J. de Pablo, and A. Yethiraj, J. Chem. Phys. **107**, 6956 (1997).
[17]S. Nosé, Mol. Phys. **52**, 255 (1984).
[18]S. Nosé, J. Chem. Phys. **81**, 511 (1984).
[19]W. G. Hoover, Phys. Rev. A **31**, 1695 (1985).
[20]J. I. Siepmann, S. Karaborni, and B. Smit, Nature (London) **365**, 330 (1993).
[21]W. L. Jorgensen, J. D. Madura, and C. J. Swenson, J. Am. Chem. Soc. **106**, 6638 (1984).
[22]M. Tuckerman, B. J. Berne, and G. J. Martyna, J. Chem. Phys. **97**, 1990 (1992).
[23]H. Flyvbjerg and H. G. Petersen, J. Chem. Phys. **91**, 461 (1989).
[24]P. Hachmann and J. Meissner, J. Rheol. **47**, 989 (2003).
[25]M. Mondello and G. S. Grest, J. Chem. Phys. **103**, 7156 (1995).
[26]J. D. Moore, S. T. Cui, H. D. Cochran, and P. T. Cummings, J. Non-Newtonian Fluid Mech. **93**, 83 (2000).
[27]M. Doi and S. F. Edwards, *The Theory of Polymer Dynamics* (Oxford University Press, New York, 1986).
[28]P. G. de Gennes, J. Chem. Phys. **55**, 572 (1971).
[29]P. E. Rouse, J. Chem. Phys. **21**, 1272 (1953).